Journal of Materials Chemistry C

ROYAL SOCIETY OF CHEMISTRY

PAPER

View Article Online
View Journal | View Issue

Cite this: J. Mater. Chem. C, 2022, 10, 4886

A deep blue thermally activated delayed fluorescence emitter: balance between charge transfer and color purity†

Bahadur Sk, Ezhakudiyan Ravindran, Upasana Deori, Nisha Yadav, Gyana Prakash Nanda and Pachaiyappan Rajamalli *

Received 19th October 2021,
Accepted 31st January 2022

DOI: 10.1039/d1tc05027c

rsc.li/materials-c

An efficient blue organic light-emitting diode (OLED) device with high color purity is a challenging issue with technological relevance. Herein, we demonstrated the role of the donor substitution position in a thermally activated delayed fluorescence (TADF) emitter to achieve deep blue emission with improved color purity without reducing the device performance. A novel (4-(3,6-di-*tert*-butyl-9*H*-carbazol-9-yl)phenyl)(6-(3,6-di-*tert*-butyl-9*H*-carbazol-9-yl)pyridin-3-yl)methanone (**3BPy-*p*DTC**) was synthesized, where two *tert*-butyl carbazolyl (DTC) donors linearly connected at the *para* position of the benzoyl pyridine (3BPy) acceptor core. The **3BPy-*p*DTC** emitter shows a low ΔE_{ST} value of 0.19 eV with a subsequent overlap between holes and electrons which leads to a high photoluminescence quantum yield (PLQY) of 93%. Besides, this emitter exhibits narrow emission spectra with a full-width at half maximum (FWHM) of 58 nm. The OLED device using the **3BPy-*p*DTC** dopant provided a high external quantum efficiency (EQE) of 25% with deep blue emission at λ_{max} of 458 nm. **3BPy-*p*DTC** shows color purity in deep blue emission as compared to its *meta* substituted counterpart (**3BPy-*m*DTC**) due to the locked geometry *via* intramolecular H-bonding and weak excited state charge transfer (CT) interactions. The current study paves the way for developing deep-blue TADF emitters with high efficiency and color purity.

1. Introduction

Metal-free organic emitters with an electron-donating (D) unit connected *via* a π-linker to an electron-accepting (A) unit emerged as important materials for optoelectronic devices.[1–4] The optical and electrochemical properties of donor–acceptor (D–A) molecules can be tuned by controlling the excited-state intramolecular charge transfer (ICT).[2,5–9] The excited-state CT proceeds with drastic conformational changes, mainly the rotation at the D–A bond leading to the formation of a twisted intramolecular charge transfer (TICT) state.[6,10] Consequently, spectral broadening, large Stokes shifts, and lowering of the bandgap are observed in CT-based organic emitters.[2,11] However, achieving high color purity in the devices is one of the critical issues due to spectral broadening.[12–14] The broadening in emission (*i.e.* full width at half maximum, FWHM) can be tuned by monitoring the CT interactions in D–A-based organic emitters.[15]

Recently, D–A based chromophores have attracted much attention due to a lower singlet (S_1)–triplet (T_1) energy gap (ΔE_{ST}), which facilitates the photon upconversion from the low-lying T_1 to the S_1 excited-state. This leads to delayed fluorescence which is commonly known as thermally activated delayed fluorescence (TADF).[1,3,16–22] Therefore, 100% internal quantum efficiency (IQE) of OLED devices can be achieved based on these metal-free TADF emitters. Hence, highly efficient, light-weight, flexible, and environment-friendly OLED devices are achievable without the use of noble metals such as Ir and Pt.[23–28] Amid several recent reports, the development of blue TADF emitters with high color purity and high efficiency remains a challenge.[12,29–32]

The decoupling of the highest occupied molecular orbital (HOMO) and the lowest unoccupied molecular orbital (LUMO) is important to reduce the ΔE_{ST}. Hence, several D–A-based TADF emitters with twisted molecular geometry were designed to separate the HOMO and LUMO and obtain a low ΔE_{ST} to promote exciton upconversion from T_1 to the S_1 excited state.[18,19] However, a more twisted structure results in the broadening of emission spectra, generally a FWHM of over

Materials Research Centre, Indian Institute of Science, CV Raman Road, Bangalore-560012, Karnataka, India. E-mail: rajamalli@iisc.ac.in

† Electronic supplementary information (ESI) available: General information, synthesis and characterization including NMR spectra, computational details, UV-Vis spectra, crystal structure, L–M plot, power and current efficiency *vs.* luminance. CCDC 2116276. For ESI and crystallographic data in CIF or other electronic format see DOI: 10.1039/d1tc05027c

100 nm, which directly impacts the color purity of the devices.[33] Conversely, a complete planar structure gives a narrow emission but it shows poor device performance due to large ΔE_{ST} values. In order to achieve high device performance with high color purity, the above trade-off needs to be solved. Therefore, an optimum molecular design strategy is required to balance the low ΔE_{ST} for efficient photon upconversion and a narrow FWHM in emission for color purity.

Recently, a multi-resonance TADF (MR-TADF) emitter was found to be an ideal molecular design for OLEDs due to its small ΔE_{ST}, high PLQY, and narrow emission.[34–37] However, nearly all MR-TADF emitters are based on boron/nitrogen, which limits the molecular design flexibility and scope of these emitters.[15,38] Further, most of the MR-TADF based emitters suffer from poor luminance.[39,40] In order to overcome this limitation, conventional TADF emitters need to be designed and focused to achieve high color purity along with high device brightness as well as performance. Recently, several attempts were made to improve color purity and device performance using conventional TADF molecular design (Table S8, ESI†).

The enhanced molecular restriction from *ortho* (*o*PTC, FWHM = 97 nm) to *meta* (*m*PTC, FWHM = 86 nm) substitution of aryl groups in the phenoxazine–benzonitrile dyad led to better color purity as reported by Zhang and coworkers.[41] Cheng and coworkers developed two isomeric TADF emitters and realised improved color purity with device performance for one isomer over the other. However, the emission maximum was in the sky-blue region and CIE_y was over 0.18, and hence the emission spectrum needs to be blue-shifted to bring down the CIE_y value below 0.15 for practical applications.[3] Further, Kieffer and coworkers demonstrated that balanced CT interactions leading to hole/electron (h/e) overlap represent the key parameter for reducing the FWHM and color purity.[42] The donor substitution at the *meta* and *para* positions to the pyridoquinoxaline (PQ) acceptor core significantly affects the CT interactions and optical properties demonstrated by Patra and coworkers.[43]

Very few attempts were made to design a conventional TADF emitter with a narrow emission bandwidth in the blue region.[44] However, a unified molecular design strategy to achieve high efficiency with color purity in the deep blue region is not clearly represented. Our group developed **3BPy-*m*DTC** as the TADF emitter in the cyan/sky-blue region by substituting donors at the *meta* position of the 3BPy acceptor core.[45] Due to a strong donor–acceptor CT interaction and decoupled HOMO–LUMO, a broad TADF emission was observed in the sky blue region (λ_{max} ~475 nm) with an EQE of 24.6%. Here, we have designed and synthesised a **3BPy-*p*DTC** TADF emitter. This newly synthesised *para*-substituted donor at the 3BPy acceptor core (**3BPy-*p*DTC**) resulted in a narrow emission (FWHM ~58 nm) in the deep blue region (λ_{max} = 458 nm) with a very high EQE of 25%. This is due to the balance between the low ΔE_{ST} and CT interactions. This suggests that fine-tuning of molecular design is very important to improve the color purity and achieve deep blue emission. This study demonstrated a unique strategy to obtain deep blue emission with improved color purity and retain the high electroluminescence device performance (Scheme 1).

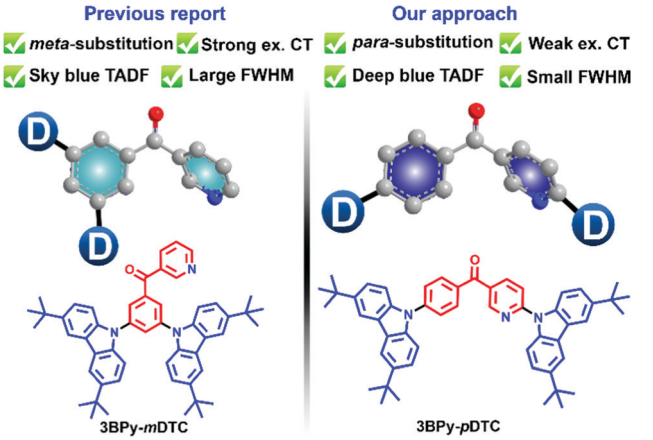

Scheme 1 Molecular design strategy of a blue TADF emitter: a comparative account of the intrinsic ICT interactions of *meta* and *para* substituted donors on the 3BPy acceptor core. The molecular structures of *meta*-substituted **3BPy-*m*DTC** and *para*-substituted **3BPy-*p*DTC** with DTC as the donor units are shown.

2. Results and discussion

2.1 Design strategy and synthesis

An earlier report for the *meta* substituted donors on the 3BPy acceptor core exhibited strong excited state charge transfer (CT) interactions.[45] As a result, sky blue (λ_{em} = 476 nm) TADF emission was observed. To develop deep blue emission with high device efficiency, we tuned the excited state CT interactions by synthesizing its positional isomer, consisting of the same terminal DTC as the donor group substituted to the *para* positions of the central phenyl ring 3BPy acceptor core. The donor substitution at the *para* positions of the 3BPy acceptor core *via* the cost-effective Ullmann cross-coupling reaction resulted in **3BPy-*p*DTC**. The details of the synthetic procedure are given in the supplementary information (Section 2, Scheme S1, ESI†). **3BPy-*p*DTC** was purified by temperature gradient high vacuum sublimation and characterized by NMR spectroscopy, high-resolution mass spectrometry and single crystal X-ray diffraction (SCXRD) analysis (Scheme S1 and Fig. S16, S17, ESI†).

2.2 DFT calculation

A time-dependent density functional theory (TDDFT) calculation was carried out using the Gaussian 09W program package. The optimized molecular structures of the two compounds are shown in Fig. 1. **3BPy-*p*DTC** shows an almost planar structure (D–A–D dihedrals, 35° and 49°, respectively) with an energy gap of 3.37 eV, whereas **3BPy-*m*DTC** shows a more twisted structure (50° and 57°) with a lowered energy gap of 3.18 eV. Therefore, **3BPy-*p*DTC** is expected to show deep blue emission in contrast to **3BPy-*m*DTC**, which is a sky-blue emitter.[45] HOMO and LUMO distributions are localized on the donor (DTC) and acceptor (3BPy), respectively, for both emitters. Notably, **3BPy-*p*DTC** shows separation between the HOMO and LUMO with a very large overlap, which leads to a large f for **3BPy-*p*DTC** (f = 0.481), and a large f is important for improving the radiative decay

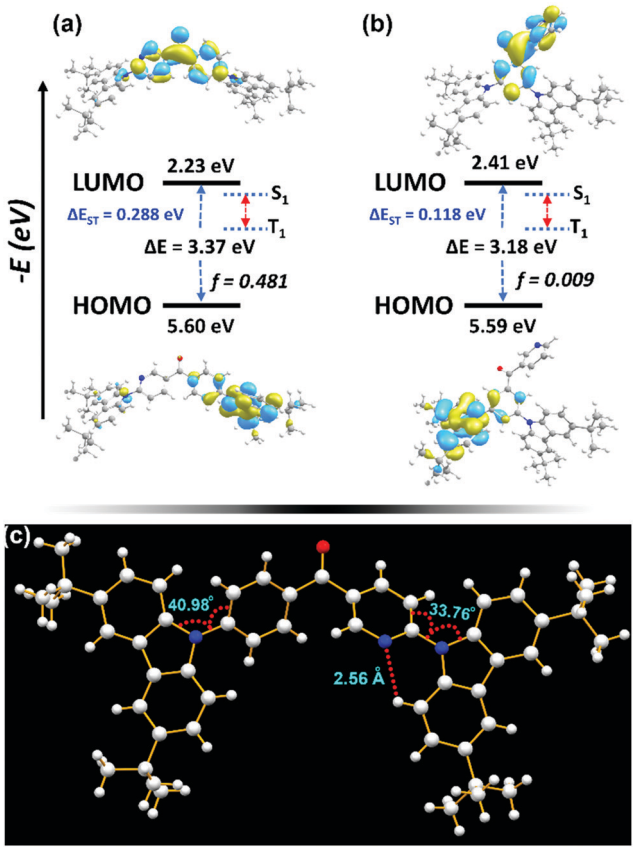

Fig. 1 DFT calculated electron density distributions of the highest occupied molecular orbital (HOMO) and the lowest unoccupied molecular orbital (LUMO) of (a) **3BPY-*p*DTC** and (b) **3BPy-*m*DTC** at the B3LYP/6-311G(d,p) level. (c) The molecular structure and packing diagram of **3BPy-*p*DTC** obtained from single crystal X-ray diffraction (SCXRD) analysis displaying the intramolecular H-bonding interaction and the donor–acceptor dihedral angles.

channel and maintain a high PLQY. In contrast to **3BPy-*m*DTC**, here the acceptor pyridine and phenyl π-spacer units are involved in both HOMO and LUMO distributions. The main transitions and oscillator strengths of both emitters are listed in Table S1 (ESI†). The excited state hole and electron distributions for S_1 and T_1 states were analyzed using *Multiwfn* software.[46] The electrons of both S_1 and T_1 are distributed mainly in the acceptor core (Fig. S1 and Table S2, ESI†). In comparison, the hole for S_1 is predominantly distributed over the donor carbazole units and extended to the phenyl π-spacer. However, the hole for T_1 is distributed throughout the molecule (Fig. S1a, ESI†).[26]

The crystal structure of **3BPy-*p*DTC** obtained from the SCXRD analysis indicates the H-bond formation between the pyridine nitrogen and adjacent H–CH of the donor carbazole unit (N···H–CH: 2.56 Å) locking the molecular geometry (Fig. 1c and Fig. S2, Table S3, ESI†). Additionally, low D–A dihedral angles of 33.76° and 40.98°, respectively (Fig. 1c), are observed due to a locked molecular structure. The DFT optimized geometry also indicates a similar trend of twisting angles (Fig. 1a). As a result, a prominent overlap/coupling between the holes and electrons for both S_1 and T_1 was observed. This facilitates the photon upconversion from the T_1 to S_1 state through reverse intersystem crossing (RISC). Comparatively, a smaller coupling of holes and electrons in S_1 and T_1 states was observed for **3BPy-*m*DTC** (Fig. S1b, ESI†). This suggests that **3BPy-*m*DTC** possesses stronger excited-state intramolecular charge transfer interactions as compared to **3BPy-*p*DTC**.

2.3 Photophysical properties

The UV-Vis absorption and PL spectra of **3BPy-*p*DTC** recorded in toluene solution are shown in Fig. 2a and Table 1. **3BPy-*p*DTC** exhibits prominent absorption broad bands at λ_{abs} = 375 nm due to the intramolecular charge transfer (ICT) absorption linked with the electron transfer from the donor (tCz) to the acceptor group (BPy). Further, the absorption measurement of **3BPy-*p*DTC** was carried out in solvents with varying polarity (Fig. S3, ESI†). There is no significant change of peak maxima and the shape of the absorption band with varying solvent polarity. The *meta*-substituted (**3BPy-*m*DTC**) isomer shows two absorption bands: the band at 350 nm is due to the π–π* transitions and the weak broad band at 382 nm is due to the weak ground state ICT from the donor to the

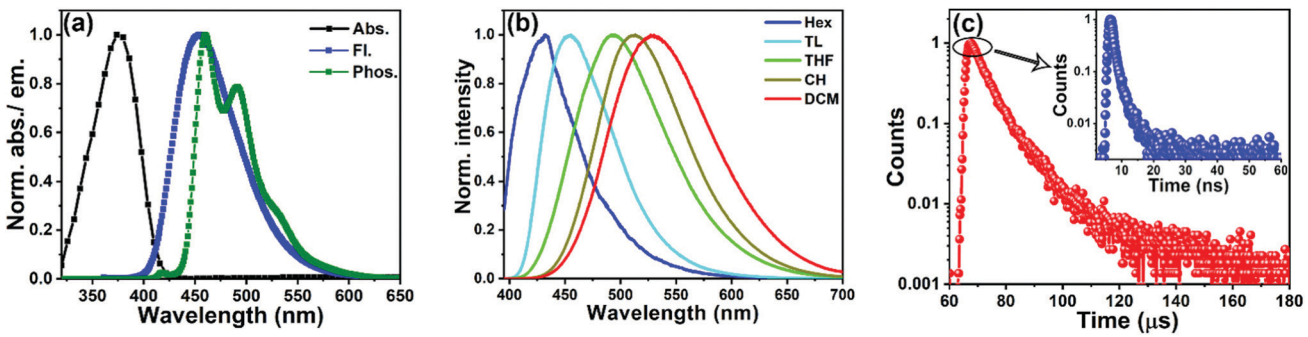

Fig. 2 (a) Normalized absorption, fluorescence (λ_{ex} = 405 nm) and phosphorescence (λ_{ex} = 405 nm) spectra of **3BPy-*p*DTC** in toluene (10 μM). (b) Normalized fluorescence (λ_{ex} = 405 nm) spectra of **3BPy-*p*DTC** in solvents of varying polarity. Hex: hexane (0.009), TL: toluene (0.099), THF: tetrahydrofuran (0.207), CH: chloroform (0.259) and DCM: dichloromethane (0.309). The solvent polarity parameter (E_T^N value) is mentioned in the parenthesis. (c) Emission decay profile (λ_{ex} = 400 nm LED source) of **3BPy-*p*DTC** in degassed toluene at room temperature showing delayed fluorescence; inset: decay (λ_{ex} = 410 nm diode laser source) at the nanosecond timescale indicating prompt fluorescence.

Table 1 Photophysical properties of **3BPy-*p*DTC** and **3BPy-*m*DTC**

Compound	λ_{abs}[a] (nm)	λ_{em}[a] (nm)	E_g[b] (eV)	HOMO[c] (eV)	LUMO[d] (eV)	ΔE_{ST}[e] (eV)	PLQY[f] (Sol/film, %)	k_r[g] (10^8 s^{-1})	k_{ISC}[h] (10^8 s^{-1})	k_{RISC}[i] (10^5 s^{-1})	$k_{nr,S}$[j] (10^7 s^{-1})
3BPy-*p*DTC	375	453	3.01	−5.86	−2.85	0.19	29/93	5.1	1.2	1.7	3.5
3BPy-*m*DTC	381	480	2.90	−5.61	−2.71	0.05	7/92	1.4	0.63	1.6	0.7

[a] Measured in toluene (10 μM) at room temperature. [b] Estimated from the onset of the absorption spectrum. [c] Measured from the oxidation potential in 1 mM DCM solution by cyclic voltammetry. [d] Calculated from HOMO–E_g. [e] $\Delta E_{ST} = E_S - E_T$, and E_S and E_T were obtained from the onset of fluorescence and phosphorescence spectra, respectively. [f] PL quantum yield evaluated in toluene using the reference dye and in the *m*CBP film with 7 wt% dopant using an integrating sphere. [g] Rate constant of fluorescence radiative decay ($S_1 \rightarrow S_0$, $k_r = \Phi_p/\tau_p$). [h] Rate constant of ISC ($S_1 \rightarrow T_1$, k_{ISC}). [i] Rate constant of RISC ($T_1 \rightarrow S_1$, k_{RISC}). [j] Rate constant of nonradiative decay in the singlet state.

acceptor (Fig. S4, ESI†).[45] As a result, a high molar extinction coefficient was obtained for the CT band of **3BPy-*p*DTC** (ε_{375nm} = 55 560 M^{-1} cm^{-1}) compared to **3BPy-*m*DTC** (ε_{385nm} = 3330 M^{-1} cm^{-1}).

The steady-state emission of **3BPy-*p*DTC** lies in the blue region and the peak is centred at 453 nm in toluene. To see the solvent effect on emission, steady-state emission spectra were measured with various polarities of the solvents (from hexane to dichloromethane (DCM)) (Fig. 2b and Fig. S5, S6, ESI†). In contrast to the absorption spectra, the emission spectra are red-shifted in polar solvents and the emission maximum changes from 434 nm in hexane to 530 nm in DCM (Fig. 2b). Both the emission maximum and the FWHM increased dramatically with solvent polarity (Table S4, ESI†). The significant solvatochromic shifts observed in the fluorescence spectra compared to no significant change in the absorption spectra suggest an excited state with a stronger ICT character and larger dipole moments relative to the ground state. The large Stokes shift and spectral broadening indicate a highly polarized ICT state.[43] Excited-state CT characteristics were probed using the Lippert–Mataga (L–M) plot for both the compounds (Section 4.3 and Fig. S7, S8, Tables S4–S6, ESI†). A larger Stokes shift and transient dipole ($\mu_E - \mu_G$) of **3BPy-*m*DTC** were observed as compared to **3BPy-*p*DTC** (Table S6, ESI†). This indicates the relatively weaker excited state CT interactions in **3BPy-*p*DTC** (Fig. S7, S8 and Table S6, ESI†).

The PLQY was measured in oxygen-free toluene solutions, the obtained quantum yield is 29% and the value decreases to 24% in the presence of oxygen (ESI,† Section 4.4). The decrease in the PLQY in the presence of oxygen supports that this emitter has TADF properties. The T_1 state of this emitter is readily quenched by triplet ground state oxygen molecules, which leads to a decrease in RISC and subsequently the photoluminescence intensity. The PLQY of 7 wt% **3BPy-*p*DTC** doped in the *m*CBP thin film is 93%, which was measured using an integrating sphere under a N_2 atmosphere (Table 1). Surprisingly, the PLQY value of the thin film is much higher than that of the solution. This is because of the strong molecular packing in the crystalline or solid phase *via* intramolecular H-bonding (C–H···N, 2.56 Å, Fig. 1c) interactions locking the molecular geometry and restricted rotation at around the D–A bond (dihedral angles, 33.76° and 40.98°, Fig. 1c). As a result, we observed a relatively higher PLQY in the solid film of **3BPy-*p*DTC** compared to the solution phase.

In order to know the nature of phosphorescence emission and ΔE_{ST}, the emission spectrum of **3BPy-*p*DTC** was measured at liquid nitrogen temperature (77 K, Fig. 2a). At room temperature, considerable emission from only the S_1 state was observed in the solution phase. On freezing the solution phase sample to 77 K, intramolecular rotations about the D–A bonds are mainly restricted due to the increased rigidity of the molecular environment. This, in turn, inhibits the nonradiative decay from T_1 and thermally activated nonradiative decay channels and results in substantial phosphorescence emission from T_1. The steady-state emission spectra, including the phosphorescence spectrum of **3BPy-*p*DTC**, are shown in Fig. 2a. Structured emission was observed in the phosphorescence spectrum of **3BPy-*p*DTC** (Fig. 2a), and this suggests that the phosphorescence emission from the LE state of T_1. The singlet and triplet energy gaps were calculated from the onset of room temperature fluorescence (S_1 = 3.01 eV) and low temperature (77 K) phosphorescence (T_1 = 2.82 eV) spectra in toluene solvent. The calculated ΔE_{ST} is 0.19 eV (Fig. 2a, Table 1 and Table S2, ESI†). A small ΔE_{ST} = 0.19 eV indicates facile photon upconversion from T_1 to S_1 RISC, leading to TADF properties.

2.4 Time-resolved spectroscopy

To confirm the TADF properties of this emitter, the transient decay of **3BPy-*p*DTC** was recorded in degassed toluene at room temperature (Fig. 2c and Table S7, ESI†). The decay profiles in the nanosecond (ns) and microsecond (μs) channels were found to be biexponential. The average lifetime (τ_{avg}) of emission decay in the nanosecond timescale is τ_{avg} = 1.5 ns, whereas the long-lived lifetime is τ_{avg} = 7.7 μs (Fig. 2c, Table 1 and Table S7, ESI†).[47] The short component is assigned to be the prompt fluorescence (PF), and the long-lived species is due to the delayed fluorescence (DF), the photon upconversion from T_1 to S_1 and subsequent radiative decay from the S_1 state. These short and long component radiative decays confirm that this emitter is in TADF nature (*vide infra*). To know the emission lifetime in the thin film, the emission spectra and transient decay of **3BPy-*p*DTC** were also recorded in 10 wt% doped PMMA matrix (Fig. S9 and Table S7, ESI†). The biexponential decay of **3BPy-*p*DTC** in the PMMA matrix with an average lifetime of τ_{avg} = 25.9 μs was observed (Fig. S9 and Table S7, ESI†).

2.5 Electrochemical and thermal properties

The electrochemical properties of **3BPy-*p*DTC** were examined using cyclic voltammetry (CV), and the results are shown in Table 1 and Fig. S10 (ESI†). The HOMO energy level was

calculated to be −5.86 eV from the oxidation potential, and the LUMO energy level was estimated to be −2.85 eV for **3BPy-*p*DTC**. The lower LUMO level of **3BPy-*p*DTC** compared to **3BPy-*m*DTC** (2.71 eV) is due to a better accumulation of charges on the acceptor part. Similarly, the higher HOMO level in **3BPy-*p*DTC** compared to **3BPy-*m*DTC** (HOMO = −5.61 eV) is due to the electron-donating carbazole units linked in the *para* position of the acceptor core, leading to the distribution of the donor electron to the acceptor through the resonance (+R) effect.[43] The electrochemical stability of **3BPy-*p*DTC** was studied in DCM solution by recording the cyclic voltammograms up to 100 cycles at a positive potential.[49,50] Fig. S11 (ESI†) shows no significant change of peak current and shape of CV traces up to 100 cycles indicating the high electrochemical stability of **3BPy-*p*DTC**. The electrochemical properties are summarized in Table 1.

The thermal properties of **3BPy-*p*DTC** were determined by thermogravimetric analysis (TGA) and differential scanning calorimetry (DSC) under a nitrogen atmosphere; the thermograms are shown in Fig. S12 (ESI†). **3BPy-*p*DTC** shows high thermal stability with thermal decomposition temperatures over 413 °C. Glass transition temperatures were measured using differential scanning calorimetry (DSC). Interestingly, **3BPy-*p*DTC** shows a higher glass transition temperature (T_g = 142 °C) as compared to **3BPy-*m*DTC** (T_g = 101 °C) due to a more rigid structure. High T_d and T_g values are important for enhanced morphological stability in the film (Fig. S12b, ESI†). Further, the photostability of the **3BPy-*p*DTC** film in PMMA was tested by the continuous irradiation of a 150 W xenon lamp (λ_{ex} = 375 nm) and the emission was recorded at λ_{em} = 455 nm for 2.5 h (Fig. S13, ESI†). The fluorescence intensity of the film remained around 85% up to 2.5 hours of continuous irradiation.

2.6 Electroluminescence performance

The multilayer OLED device was fabricated using **3BPy-*p*DTC** as the emissive layer to examine the electroluminescence performance and a comparison study of its *meta* counterpart of **3BPy-*m*DTC** was performed. The OLED devices were fabricated using these materials as dopants with the following structures: ITO/NPB (30 nm)/TAPC (20 nm)/mCBP (10 nm)/*m*CBP:**3BPy-*p*DTC** (7 wt%) or **3BPy-*m*DTC** (7 wt%) (30 nm)/DPEPO (5 nm)/TmPyPb (60 nm)/LiF (0.8 nm)/Al (100 nm) (Fig. 3a and b).[48,49] The electroluminescence (EL) properties of these two emitters are summarized in Fig. 3 and Table 2. The EQE–luminance curves reveal a maximum EQE (EQE_{max}) of 25.3% for the **3BPy-*p*DTC** device and 24.6% for the **3BPy-*m*DTC** (Fig. 3c and d). Although both emitters show comparable EQEs, the EL spectra show deep blue emission for **3BPy-*p*DTC** at λ_{em} = 458 nm with very good color purity (FWHM = 58 nm) compared to sky blue emission for the **3BPy-*m*DTC** device (λ_{em} = 476 nm) with a relatively broad emission band (FWHM = 66 nm) (Fig. 4 and Table 2). The CIE coordinates are (0.14, 0.13) for **3BPy-*p*DTC** and (0.15, 0.28) for **3BPy-*m*DTC** at 8 V. The **3BPy-*p*DTC** based device shows a high brightness of 4568 cd m^{-2}, which is much higher than that of the reported MR-TADF based OLED device (less than 1000 cd m^{-2}).[34] Interestingly, this device shows reduced roll-off as compared to the MR-TADF device and the device retains EQEs of 15.2% and 10.4% at 100 cd m^{-2} and 500 cd m^{-2}, respectively. The reduced

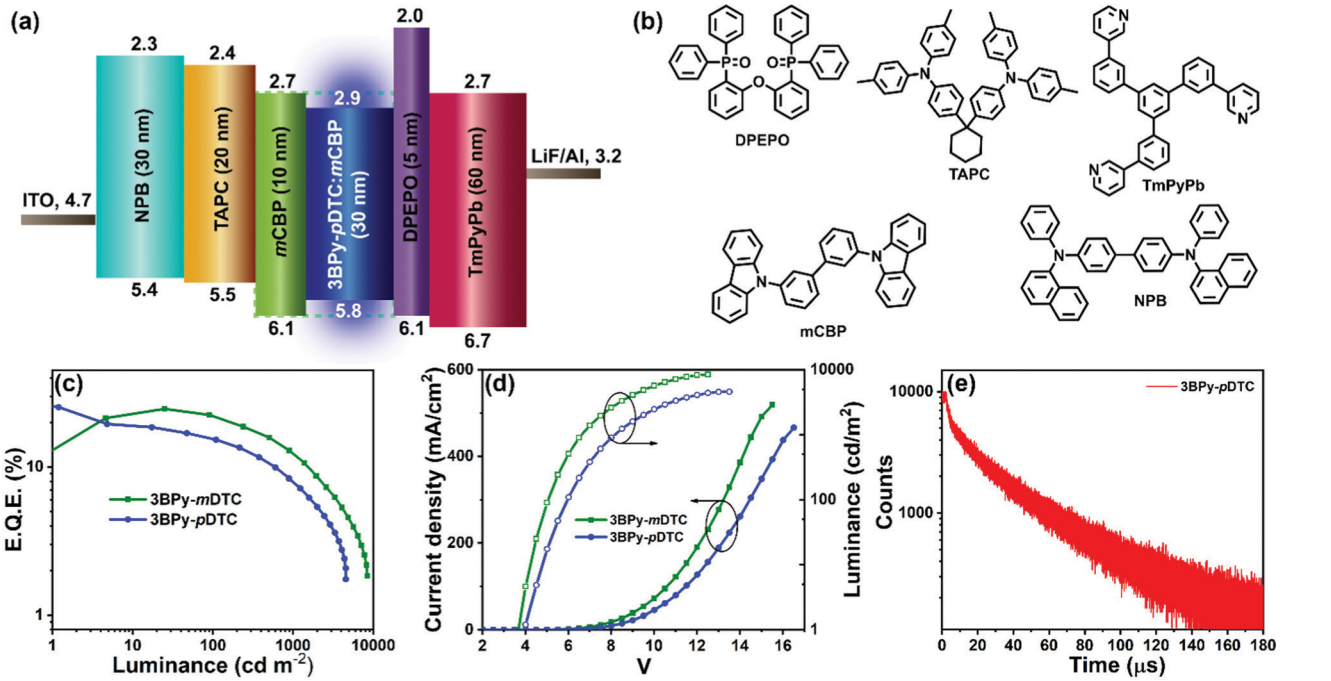

Fig. 3 OLED device fabrication: (a) device architecture, (b) molecular structure of the materials used in the device, (c) luminance *vs.* EQE, (d) current density and luminance *vs.* driving voltage and (e) transient electroluminescence characteristics of the **3BPy-*p*DTC** device.

Table 2 Electroluminescence performance of **3BPy-*p*DTC** and **3BPy-*m*DTC**

Device[a]	Turn-on voltage[b] (V)	EQE[c] (%)	Luminance, Cd m^{-2} [d] (V)	CE[e] (Cd A^{-1})	PE[f] (lm W^{-1})	CIE[g] (8 V)	EL[h] (λ^{max}) (nm)	FWHM[i] (nm)
3BPy-*p*DTC	3.8	25.3 (4.0)	4568 (13.5)	29.6	23.2	(0.14, 0.13)	458	58
3BPy-*m*DTC	3.6	24.6 (4.5)	8637 (12.5)	48.4	38.0	(0.16, 0.29)	477	66

[a] Device configurations: ITO/NPB (30 nm)/TAPC (20)/*m*CBP (10)/*m*CBP:**3BPy-pDTC** 7 wt%) or **3BPy-*m*DTC** (7 wt%) (30 nm)/DPEPO (5 nm)/TmPyPb (60)/LiF (0.8 nm)/Al (100 nm). [b] Operating voltage at a brightness of 1 cd m^{-2}. [c] Maximum external quantum efficiency (EQE). [d] Luminance. [e] CE = maximum current efficiency. [f] PE = maximum power efficiency. [g] Commission Internationale de l'éclairage (CIE) coordinates. [h] EL = electroluminescence (λ_{max} = wavelength at which the EL spectrum has the highest intensity. [i] FWHM is the full width at half maximum of EL spectra.

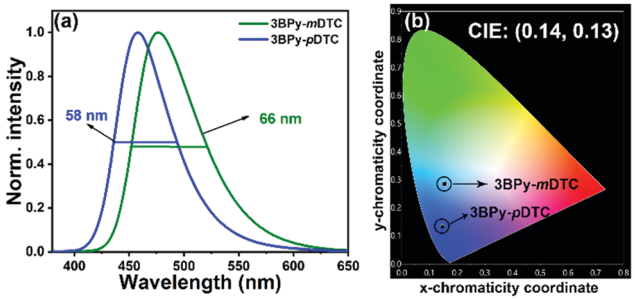

Fig. 4 Blue OLED device based on TADF emitters: (a) electroluminescence (EL) spectra and (b) CIE chromaticity diagram of **3BPy-*p*DTC** and **3BPy-*m*DTC** depicting the color purity based on the narrow FWHM and CIE coordinates towards pure blue emission.

device efficiency roll-off of **3BPy-*p*DTC** based devices is due to a small delayed fluorescence lifetime (τ_{DF} = 7.7 μs) and a fast k_{RISC} rate (k_{RISC} = 1.7 × 10^5 S^{-1}). The maximum current and power efficiencies are 29.6 cd A^{-1} and 23.2 lm W^{-1}, respectively, and these values are also higher than those of reported MR-TADF emitters.[34,35] The transient electroluminescence decay of the **3BPy-*p*DTC** device was recorded to confirm the long-lived species originating from efficient reverse intersystem crossing leading to TADF emission (Fig. 3e). Further, electroluminescence spectra were measured at various operating voltages (6–12 V, Fig. S14, ESI†). Both devices show similar emission spectra, and no residual emission is observed even at 12 V. This suggests that the device is very stable and recombination remains within the emissive layer at various operating voltages (Fig. 4, Fig. S14, S15, ESI† and Table 2).

Despite the cross-conjugation in the *meta* substituted donors on the 3BPy acceptor, we observed stronger excited-state charge-transfer interactions in **3BPy-*m*DTC** than the *para*-substituted isomer **3BPy-*p*DTC**. Consequently, a smaller Stokes shift in all polar mediums along with a prominent hole–electron overlap was observed for **3BPy-*p*DTC**. The intramolecular H-bonding (N···H–CH, 2.56 Å, Fig. 1c) plays a crucial role in locking the molecular geometry *via* restricted rotation in the D–A bond (dihedral angles, 33.76° and 40.98°, Fig. 1c) in *para*-substituted **3BPy-*p*DTC**. As a result, the less D–A twist led to diminished excited state CT, and a higher ΔE_{ST} value for **3BPy-*p*DTC** (0.19 eV) compared to **3BPy-*m*DTC** (0.05 eV) was observed. However, both emitters exhibit almost similar electroluminescence performance with different λ_{max} and spectral broadness. Thus, for better device performance with color purity, the overlap between holes and electrons is equally important, along with low ΔE_{ST} values for facile RISC. Further, the balanced CT interactions are also the key parameter to reduce the FWHM.[42] Therefore, a combination of lowering excited state CT interactions through an appropriate donor position and the locking of molecular geometry resulted in deep blue TADF emission with a narrow bandwidth for *para*-substituted **3BPy-*p*DTC**. In addition, the participation of the T_2 state along with the T_1 state in RISC leads to high device performance for both the emitters (Fig. S1, ESI†). The small energy gaps of T_1–T_2 ($\Delta E_{T_2-T_1}$ = 0.054 eV) and S_1–T_2 ($\Delta E_{S_1-T_2}$ = 0.234 eV) in **3BPy-*p*DTC** facilitate the spin upconversion through reverse internal conversion (RIC) and RISC, respectively. The high-performance deep blue OLED device based on **3BPy-*p*DTC** opens up a new avenue for further developing pure blue TADF emitters and provides scope for practical applications in flat panel displays.

3. Conclusions

In summary, two positional isomers (**3BPy-*p*DTC** and **3BPy-*m*DTC**) were synthesised and the effects on the emission maximum, color purity, and device performance were studied. Both emitters show TADF properties with high PLQYs over 90%. However, the *para* substituted emitter (**3BPy-*p*DTC**) leads to higher color purity with deep-blue emission compared to the *meta* counterpart (**3BPy-*m*DTC**). The OLED device using the **3BPy-*p*DTC** dopant provided a high EQE of 25% with narrow (FWHM = 58 nm) emission at λ_{em} = 458 nm and CIE coordinates of 0.14, 0.13. The *para*-substituted donor on the 3BPy core (**3BPy-*p*DTC**) shows a narrow emission band due to weak charge-transfer (CT) interactions and locked geometry *via* intramolecular H-bonding. The current study demonstrated new avenues for developing narrow, deep blue OLED devices with high efficiency for practical applications.

Conflicts of interest

There are no conflicts to declare.

Acknowledgements

The authors are grateful to Prof. Chien-Hong Cheng, National Tsing Hua University, Taiwan, for providing OLED device fabrication and characterization facilities. Bahadur thanks the Indian Institute of Science (IISc) Bangalore, India, for IoE C. V. Raman Fellowship. G. P. N. thanks the Council of Scientific &

Industrial Research (CSIR) India for the Junior Research Fellowship (JRF). P. R. thanks the IISc for generous financial support and the Science & Engineering Research Board (SERB), India, for the SERB-Power Grant (SPG) (Grant no: SPG/2020/000107). We are thankful to Mr Rajendra Prasad and Mr Sarvesh of IISc for helping in recording the emission spectra and electrochemical studies, respectively.

Notes and references

1 H. Uoyama, K. Goushi, K. Shizu, H. Nomura and C. Adachi, *Nature*, 2012, **492**, 234–238.
2 S. Sasaki, G. P. C. Drummen and G. Konishi, *J. Mater. Chem. C*, 2016, **4**, 2731–2743.
3 P. Rajamalli, N. Senthilkumar, P. Y. Huang, C. C. Ren-Wu, H. W. Lin and C. H. Cheng, *J. Am. Chem. Soc.*, 2017, **139**, 10948–10951.
4 Y. Liu, C. Li, Z. Ren, S. Yan and M. R. Bryce, *Nat. Rev. Mater.*, 2018, **3**, 18020.
5 H. Tsujimoto, D. G. Ha, G. Markopoulos, H. S. Chae, M. A. Baldo and T. M. Swager, *J. Am. Chem. Soc.*, 2017, **139**, 4894–4900.
6 C. J. Chen, R. J. Huang, A. S. Batsanov, P. Pander, Y. T. Hsu, Z. G. Chi, F. B. Dias and M. R. Bryce, *Angew. Chem., Int. Ed.*, 2018, **57**, 16407–16411.
7 X. Tang, L. S. Cui, H. C. Li, A. J. Gillett, F. Auras, Y. K. Qu, C. Zhong, S. T. E. Jones, Z. Q. Jiang, R. H. Friend and L. S. Liao, *Nat. Mater.*, 2020, **19**, 1332–1338.
8 N. Altinolcek, A. Battal, C. N. Vardalli, M. Tavasli, H. A. Yu, W. J. Peveler and P. J. Skabara, *J. Mol. Struct.*, 2021, **1239**, 130494.
9 B. Sk, V. Thangaraji, N. Yadav, G. P. Nanda, S. Das, G. Parthasarathy, E. Zysman-Colman and P. Rajamalli, *J. Mater. Chem. C*, 2021, **9**, 15583–15590.
10 R. S. Nobuyasu, J. S. Ward, J. Gibson, B. A. Laidlaw, Z. Ren, P. Data, A. S. Batsanov, T. J. Penfold, M. R. Bryce and F. B. Dias, *J. Mater. Chem. C*, 2019, **7**, 6672–6684.
11 H. Tanaka, K. Shizu, H. Nakanotani and C. Adachi, *Chem. Mater.*, 2013, **25**, 3766–3771.
12 C.-Y. Chan, M. Tanaka, Y.-T. Lee, Y.-W. Wong, H. Nakanotani, T. Hatakeyama and C. Adachi, *Nat. Photonics*, 2021, **15**, 203–207.
13 G. Hong, X. Gan, C. Leonhardt, Z. Zhang, J. Seibert, J. M. Busch and S. Braese, *Adv. Mater.*, 2021, **33**, 2005630.
14 S. Oda, W. Kumano, T. Hama, R. Kawasumi, K. Yoshiura and T. Hatakeyama, *Angew. Chem., Int. Ed.*, 2021, **60**, 2882–2886.
15 J.-M. Teng, Y.-F. Wang and C.-F. Chen, *J. Mater. Chem. C*, 2020, **8**, 11340–11353.
16 L. Sarala, R. Babu Yathirajula, P. Gopikrishna, E. Elaiyappillai, A. Bella, S. Sundar Manoharan, P. Krishnan Iyer and P. M. Johnson, *J. Photochem. Photobiol.*, 2018, **365**, 232–237.
17 Y. Tao, K. Yuan, T. Chen, P. Xu, H. Li, R. Chen, C. Zheng, L. Zhang and W. Huang, *Adv. Mater.*, 2014, **26**, 7931–7958.
18 Y. Im, M. Kim, Y. J. Cho, J.-A. Seo, K. S. Yook and J. Y. Lee, *Chem. Mater.*, 2017, **29**, 1946–1963.
19 M. Y. Wong and E. Zysman-Colman, *Adv. Mater.*, 2017, **29**, 1605444.
20 E. W. Evans, Y. Olivier, Y. Puttisong, W. K. Myers, T. J. H. Hele, S. M. Menke, T. H. Thomas, D. Credgington, D. Beljonne, R. H. Friend and N. C. Greenham, *J. Phys. Chem. Lett.*, 2018, **9**, 4053–4058.
21 D. Barman, R. Gogoi, K. Narang and P. K. Iyer, *Front. Chem.*, 2020, **8**, 483.
22 P. Rajamalli, D. Chen, S. M. Suresh, Y. Tsuchiya, C. Adachi and E. Zysman-Colman, Eur, *J. Org. Chem.*, 2021, 2285–2293.
23 K. Kawasumi, T. Wu, T. Y. Zhu, H. S. Chae, T. Van Voorhis, M. A. Baldo and T. M. Swager, *J. Am. Chem. Soc.*, 2015, **137**, 11908–11911.
24 W. Huang, M. Einzinger, T. Zhu, H. S. Chae, S. Jeon, S.-G. Ihn, M. Sim, S. Kim, M. Su, G. Teverovskiy, T. Wu, T. Van Voorhis, T. M. Swager, M. A. Baldo and S. L. Buchwald, *Chem. Mater.*, 2018, **30**, 1462–1466.
25 S. Jhulki, M. W. Cooper, S. Barlow and S. R. Marder, *Mater. Chem. Front.*, 2019, **3**, 1699–1721.
26 L.-S. Cui, A. J. Gillett, S.-F. Zhang, H. Ye, Y. Liu, X.-K. Chen, Z.-S. Lin, E. W. Evans, W. K. Myers, T. K. Ronson, H. Nakanotani, S. Reineke, J.-L. Bredas, C. Adachi and R. H. Friend, *Nat. Photonics*, 2020, **14**, 636–642.
27 R. Keruckiene, M. Guzauskas, L. Lapienyte, J. Simokaitiene, D. Volyniuk, J. Cameron, P. J. Skabara, G. Sini and J. V. Grazulevicius, *J. Mater. Chem. C*, 2020, **8**, 14186–14195.
28 H. Min, I. S. Park and T. Yasuda, *Angew. Chem., Int. Ed.*, 2021, **60**, 7643–7648.
29 Y. Wada, Y. Wakisaka and H. Kaji, *ChemPhysChem*, 2021, **22**, 625–632.
30 T.-A. Lin, T. Chatterjee, W.-L. Tsai, W.-K. Lee, M.-J. Wu, M. Jiao, K.-C. Pan, C.-L. Yi, C.-L. Chung, K.-T. Wong and C.-C. Wu, *Adv. Mater.*, 2016, **28**, 6976–6983.
31 J.-H. Lee, C.-H. Chen, P.-H. Lee, H.-Y. Lin, M.-K. Leung, T.-L. Chiu and C.-F. Lin, *J. Mater. Chem. C*, 2019, **7**, 5874–5888.
32 G. Xia, C. Qu, Y. Zhu, J. Ye, K. Ye, Z. Zhang and Y. Wang, *Angew. Chem., Int. Ed.*, 2021, **60**, 9598–9603.
33 J. R. Lakowicz, *Principles of Fluorescence Spectroscopy*, Springer, New York, 2006.
34 T. Hatakeyama, K. Nakajima, S. Nakatsuka, K. Kinoshita, T. Hatakeyama, K. Shiren, S. Nomura, J. Ni, Y. Ono and T. Ikuta, *Adv. Mater.*, 2016, **28**, 2777–2781.
35 Y. Zhang, D. Zhang, J. Wei, Z. Liu, Y. Lu and L. Duan, *Angew. Chem., Int. Ed.*, 2019, **58**, 16912–16917.
36 Y. Kondo, K. Yoshiura, S. Kitera, H. Nishi, S. Oda, H. Gotoh, Y. Sasada, M. Yanai and T. Hatakeyama, *Nat. Photonics*, 2019, **13**, 678–682.
37 S. M. Suresh, E. Duda, D. Hall, Z. Yao, S. Bagnich, A. M. Z. Slawin, H. Bässler, D. Beljonne, M. Buck, Y. Olivier, A. Köhler and E. Zysman-Colman, *J. Am. Chem. Soc.*, 2020, **142**, 6588–6599.
38 J. M. Ha, S. H. Hur, A. Pathak, J.-E. Jeong and H. Y. Woo, *NPG Asia Mater.*, 2021, **13**, 53.
39 S. Madayanad Suresh, D. Hall, D. Beljonne, Y. Olivier and E. Zysman-Colman, *Adv. Funct. Mater.*, 2020, **30**, 1908677.
40 F. Huang, K. Wang, Y.-Z. Shi, X.-C. Fan, X. Zhang, J. Yu, C.-S. Lee and X.-H. Zhang, *ACS Appl. Mater. Interfaces*, 2021, **13**, 36089–36097.

41 D. Y. Chen, W. Liu, C. J. Zheng, K. Wang, F. Li, S. L. Tao, X. M. Ou and X. H. Zhang, *ACS Appl. Mater. Interfaces*, 2016, **8**, 16791–16798.
42 R. Ansari, W. Shao, S. J. Yoon, J. Kim and J. Kieffer, *ACS Appl. Mater. Interfaces*, 2021, **13**, 28529–28537.
43 B. Sk, S. Khodia and A. Patra, *Chem. Commun.*, 2018, **54**, 1786–1789.
44 H. Lim, H. J. Cheon, S.-J. Woo, S.-K. Kwon, Y.-H. Kim and J.-J. Kim, *Adv. Mater.*, 2020, **32**, 2004083.
45 P. Rajamalli, V. Thangaraji, N. Senthilkumar, C.-C. Ren-Wu, H.-W. Lin and C.-H. Cheng, *J. Mater. Chem. C*, 2017, **5**, 2919–2926.
46 T. Lu and F. Chen, *J. Comput. Chem.*, 2012, **33**, 580–592.
47 B. Sk, S. Sharma, A. James, S. Kundu and A. Patra, *J. Mater. Chem. C*, 2020, **8**, 12943–12950.
48 J.-J. Lin, W.-S. Liao, H.-J. Huang, F.-I. Wu and C.-H. Cheng, *Adv. Funct. Mater.*, 2008, **18**, 485–491.
49 P. Rajamalli, N. Senthilkumar, P. Gandeepan, P.-Y. Huang, M.-J. Huang, C.-Z. Ren-Wu, C.-Y. Yang, M.-J. Chiu, L.-K. Chu, H.-W. Lin and C.-H. Cheng, *J. Am. Chem. Soc.*, 2016, **138**, 628–634.
50 B. Sk, M. Sarkar, K. Singh, A. Sengupta and A. Patra, *Chem. Commun.*, 2021, **57**, 13590–13593.